

Title:

**Epitaxial Monolayers of the Magnetic 2D Semiconductor FeBr₂
Grown on Au(111)**

Author(s):

Sebastien E. Hadjadj, Carmen González-Orellana, James Lawrence, Djuro Bikaljević, Marina Peña-Díaz, Pierluigi Gargiani, Lucia Aballe, Jan Naumann, Miguel Ángel Niño, Michael Foerster, Sandra Ruiz-Gómez, Sangeeta Thakur, u.a.







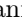


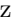

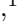


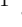
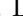
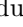


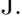

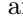

Document type: Postprint

Terms of Use: Copyright applies. A non-exclusive, non-transferable and limited right to use is granted. This document is intended solely for personal, non-commercial use.

Citation:

"Sebastian E. Hadjadj u.a., Chem. Mater. 2023, 35, 23, 9847–9856 ; <https://doi.org/10.1021/acs.chemmater.3c00978>"
Archiviert unter <http://dx.doi.org/10.17169/refubium-43076>

Epitaxial monolayers of magnetic 2D semiconductor FeBr₂ grown on Au(111)

S. E. Hadjadj ^{1,*} C. González-Orellana ^{2,*} J. Lawrence ³ D. Bikaljević ^{4,5} M. Peña-Díaz ² P. Gargiani ⁶ L. Aballe ⁶ J. Naumann ⁷ M. Á. Niño ⁶ M. Foerster ⁶ S. Ruiz-Gómez ⁸ S. Thakur ¹ I. Kumberg ¹ J. Taylor ^{9,10} J. Hayes ¹ J. Torres ¹ C. Luo ^{9,10} F. Radu ⁹ D. G. de Oteyza ^{3,11} W. Kuch ¹ J. I. Pascual ^{4,12} C. Rogero ^{2,3} and M. Ilyn ^{2,†}

¹*Freie Universität Berlin, Institut für Experimentalphysik, Arnimallee 14, 14195 Berlin, Germany*

²*Centro de Física de Materiales (CSIC/UPV-EHU), 20018 Donostia-San Sebastián, Spain*

³*Donostia International Physics Center, 20018 Donostia-San Sebastián, Spain*

⁴*CIC nanoGUNE-BRTA, 20018 Donostia-San Sebastián, Spain*

⁵*Institute of Physical Chemistry, University of Innsbruck, Innrain 52c, A-6020 Innsbruck, Austria*

⁶*ALBA Synchrotron Light Source, 08290 Barcelona, Spain*

⁷*Freie Universität Berlin, Dahlem Center for Complex Quantum Systems, Arnimallee 14, 14195 Berlin, Germany*

⁸*Max Planck Institute for Chemical Physics of Solids, 01180, Dresden, Germany*

⁹*Helmholtz-Zentrum Berlin, Albert-Einstein-Str. 15, 12489 Berlin, Germany*

¹⁰*Fakultät für Physik, Technische Universität München,*

James-Frank-Straße 1, 85748 Garching bei München, Germany

¹¹*Nanomaterials and Nanotechnology Research Center (CINN), CSIC-UNIOVI-PA, Oviedo, Spain*

¹²*Ikerbasque, Basque Foundation for Science, 48013 Bilbao, Spain*

(Dated: September 18, 2023)

Magnetic two-dimensional (2D) semiconductors have attracted a lot of attention because modern preparation techniques are capable of providing single crystal films of these materials with precise control of thickness down to the single-layer limit. It opens up a way to study rich variety of electronic and magnetic phenomena with promising routes towards potential applications. We have investigated the initial stages of epitaxial growth of the magnetic van der Waals semiconductor FeBr₂ on a single-crystal Au(111) substrate by means of low-temperature scanning tunneling microscopy, low-energy electron diffraction, x-ray photoemission spectroscopy, low-energy electron emission microscopy and x-ray photoemission electron microscopy. Magnetic properties of the one- and two-layer thick films were measured via x-ray absorption spectroscopy/x-ray magnetic circular dichroism. Our findings show a striking difference in the magnetic behaviour of the single layer of FeBr₂ and its bulk counterpart, which can be attributed to the modifications in the crystal structure due to the interaction with the substrate.

INTRODUCTION

Integration of two-dimensional (2D) materials in technologically relevant applications requires atomic-scale control of the growth of single crystalline, monolayer-thick films. Meanwhile many semiconducting 2D materials like graphene, h-BN or MoS₂ are routinely grown on the wafer scale [1], preparation of magnetic 2D materials is still limited in most cases to micromechanical exfoliation [2–10]. Prominent exceptions of this trend are magnetic transition-metal tri- and dihalides, for which single-layer growth was demonstrated recently via molecular beam epitaxy [11, 12]. In contrast to well-studied trihalides, particularly CrI₃ and CrBr₃ [2, 13–15], experimental investigation of the 2D dihalides is less advanced, although their bulk magnetic properties were thoroughly studied [16].

Bulk FeBr₂ is a layered crystal that consists of covalently bonded layers stacked via van der Waals (vdW) interactions in the CdI₂-type structure (P3m1 space group). The layers consist of triangular lattices of cations in edge-sharing octahedral coordination 1T (or D_{3d})-MX₂ structure, forming one transition metal layer sandwiched between two halide layers [16, 17]. The lateral lattice con-

stant was found to be 3.776 Å [18, 19]. Indirect Fe-Fe exchange interaction gives rise to the collinear intralayer ferromagnetic order below $T_N = 14.2$ K with out of plane (OOP) anisotropy, meanwhile the interlayer exchange is antiferromagnetic. Application of an external magnetic field of 3.15 T triggers a metamagnetic phase transition [16, 20]. The six 3d electrons of the Fe²⁺ ions are distributed between two groups of orbitals, t_{2g} (d_{xy} , d_{xz} and d_{yz}) and e_g ($d_{x^2-y^2}$, and d_{z^2}), giving rise to a magnetic moment of $4.4 \pm 0.7 \mu_B/\text{Fe atom}$ [21], which exceeds the value of $4.0 \mu_B/\text{Fe atom}$ predicted by Hund's rule [22, 23]. Various attempts of DFT calculations yield comparable values of the magnetic moments and provide useful insights on the details of the band structure [24–26].

In this work we use sublimation of the stoichiometric powder to grow epitaxial films of magnetic semiconductor FeBr₂, which belongs to the family of transition metal dihalides (TMDH) [16], on the single crystal Au(111). Feasibility of growth of TMDH films via Chemical Vapor Deposition (CVD) has been demonstrated recently [27]. In contrast to CVD, Molecular Beam Epitaxy (MBE) does not require heating of the substrate above room temperature which makes it compatible with resist-based

nanofabrication and opens up a way to the integration of the TMDH thin films in the scalable manufacturing processes. We focus our investigation on the properties of the one- and two-slab thick films employing spectroscopic and microscopic characterisation, including synchrotron-based techniques. In particular, we demonstrate the modification of the magnetic properties of the stoichiometric FeBr_2 due to a reconstruction in the first slab.

EXPERIMENT AND METHODS

FeBr_2 layers with variable thicknesses, ranging from sub-monolayer (sub-ML) to more than one monolayer, were grown on Au(111) using FeBr_2 powder from Sigma Aldrich with a purity of 98% and a Knudsen cell evaporator. The sublimation temperature for FeBr_2 was around 400 °C in ultra high vacuum (UHV) (with an evaporation pressure of 10^{-8} mbar to 10^{-9} mbar). The substrate was kept at room temperature during sublimation. A quartz microbalance was used to measure the nominal amount of the deposited material, meanwhile the calibration of the absolute thickness was done via cross-correlation of scanning tunneling microscopy (STM) images with low energy electron diffraction (LEED) data. This calibration was translated to the integral of the non-polarized soft X-ray absorption at the Fe $L_{3,2}$ edges for comparison to samples prepared in different synchrotron radiation sources. The thickness calibration procedure is shown in the supplementary information in Fig. S2. The Au(111) substrate was cleaned by standard Ar^+ sputtering and annealing cycles. Low-temperature STM (LT-STM) experiments were performed at 4.3 K (for a sub-ML sample) and at 77 K for the thicker samples at Centro de Física de Materiales and BOREAS beamline, respectively.

X-ray photoelectron spectroscopy (XPS) measurements were carried out with a Phoibos 100 photoelectron spectrometer, using a non-monochromatic Al- $K\alpha$ X-ray source. The analyser energy resolution is 0.1 eV. UHV was preserved during all the sample transfers (base pressure during experiment was 10^{-10} mbar).

X-ray magnetic circular dichroism (XMCD) measurements were performed at both the VEKMAG station (dipole-beamline) of BESSY II in Berlin [28] and the BOREAS beamline (undulator-beamline) at ALBA Synchrotron Light Facility [29]. The measurements at VEKMAG were performed by keeping the beam polarization constant and changing the field. At BOREAS we kept the field constant and changed the polarization. Absorption spectra at the Fe $L_{3,2}$ -edges were acquired at normal incidence (NI/0°, out of plane) and grazing incidence (GI/70°, in plane), applying a variable magnetic field up to ± 6 T. The temperature during the measurements at the VEKMAG beamline was set to 10 K, which is around 12.6 K and at BOREAS 2 ± 0.5 K. One 0.6-ML sample of FeBr_2 was brought by a Ferrovac suitcase to BOREAS

beamline to cross-correlate the coverage of the samples measured in the home laboratory and in the synchrotron beamlines. A control sample with similar coverage was grown in-situ and characterized at the BOREAS beamline. XAS/XMCD measurements did not show substantial differences between the samples.

The LEED images were acquired to observe the growth and the thickness-dependent change in the structure. Imaging at the mesoscopic scale was done by low-energy electron microscopy (LEEM) and x-ray photoemission electron microscopy (XPEEM) at the CIRCE beamline (ALBA Synchrotron Light Facility) [30].

RESULTS AND DISCUSSION

Epitaxial Growth of FeBr_2

The initial stage of growth of FeBr_2 films on single crystal Au(111) was studied by means of surface-sensitive electron diffraction and scanning tunneling microscopy. LEED patterns measured at 137 eV demonstrate a variation of the crystal structure of FeBr_2 with increasing number of deposited layers (Fig. 1 (a-c)). The hexagonal pattern characteristic of the clean Au(111) surface becomes attenuated and a new hexagonal pattern with smaller period and the same orientation appears when 0.6-ML of FeBr_2 is grown. An additional complex pattern of multiple dots surrounding the first-order spots of Au(111) is indicative for a surface reconstruction process that is depicted in the atomically resolved STM image (Fig. 3). In the LEED pattern acquired for the 2-ML sample, the Au(111) signal is barely visible and the reconstruction-related superstructure is strongly attenuated. At this coverage the hexagonal pattern of the ordered FeBr_2 becomes a dominant motif, also seen as second-order diffraction spots. This behaviour is characteristic of epitaxial, close to layer-by-layer growth of the overlayers on single-crystal substrates. The large-scale STM image shown in Fig. 1 (d) (see also Fig. S5) demonstrates that the islands of FeBr_2 have triangular shapes and well-defined common directions of the symmetry axes. It corroborates well with the ordered epitaxial growth inferred from the LEED diffraction patterns. One can distinguish large areas of the same thickness and limited amount of exposed atomic planes that discards a 3D growth mode. However, in the sample with nominal amount of 2.0-ML, there is nucleation of islands of the third layer and, at the same time, some voids exposing the first layer, which leads to the conclusion that the growth does not proceed in a perfect layer-by-layer mode. Fig. 1 (d) shows also islands of FeBr_2 that grow over the atomic step of the substrate. This behaviour was reported earlier for a number of different 2D materials [31–34].

The chemical composition of the films was probed using

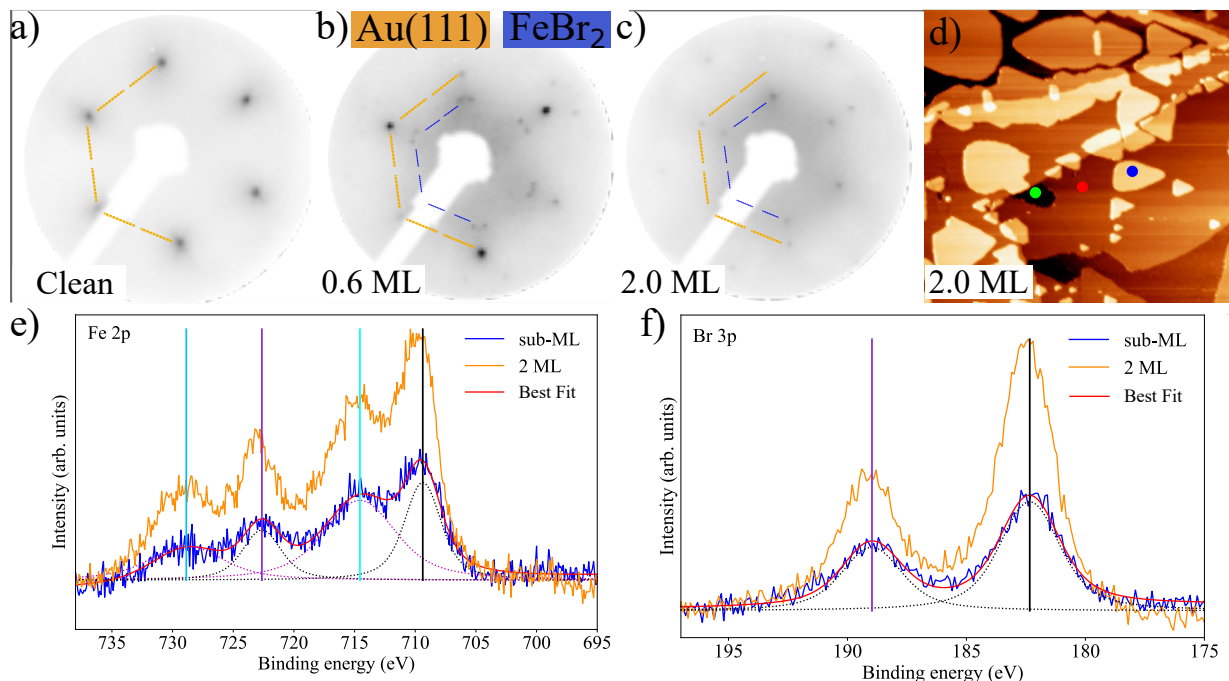


FIG. 1. (a-c) LEED images at 137 eV of a) clean Au(111), b) sub-monolayer (0.6-ML) and c) bilayer (2-ML) of FeBr₂ on Au(111). The orange half hexagon is used to designate the pattern of Au(111) and the blue half hexagon marks the pattern from FeBr₂. d) Zoomed-in part of the STM image (Fig. S5) of the 2.0-ML FeBr₂/Au(111), ($T=77$ K, $U_{\text{Bias}} = 1$ V and $I_{\text{TC}} = 0.02 \cdot 10^{-9}$ A) measured at the BOREAS beamline. The image size is 129.9×129.9 nm². In one of the terraces we appended green, red and blue spots to indicate the levels corresponding to the first, second and third ML of FeBr₂, respectively. e-f) XPS spectra of 0.6 ML and 2 ML of FeBr₂/Au(111) showing the Fe 2p and Br 3p core levels.

XPS measurements. Survey spectra (not shown) show no traces of oxygen or other contamination. The Fe 2p and Br 3p spectra acquired for the 0.6-ML and the 2.0-ML samples as well as the calculated best-fitting curves are represented in Fig. 1 (e-f). For the data evaluation, a Shirley background was subtracted and the peaks were fitted with a combination of Voigt functions (Python lmfit routine [35]). The shape of the Fe 2p spectra closely resembles the spectrum of Fe²⁺ reported for thin insulating films of FeO [36, 37] and FeCl₂ [38]. In total, four Voigt profiles were needed to fit these spectra: two for the main Fe²⁺ peaks and two for the satellite peaks. The main peaks of the Fe 2p core level are located at a binding energy of 709.4 eV for Fe 2p_{3/2} and 722.6 eV for Fe 2p_{1/2} with a spin orbit (SO) splitting of ~ 13 eV, in close accordance with the data reported in literature [36]. The satellites are associated to the final-state effect and are related to the multiplet structure of the 2p transition metal core level [39]. The Br 3p doublet is similar to the spectrum reported for Br¹⁻ in KBr and the position of the peaks falls in the same range of energies [40]. For further information about the fitting parameters see table S1. Both Fe 2p and Br 3p spectra have the same shape for the 0.6-ML and the 2.0-ML samples. In contrast to the situation observed for NiBr₂, XPS spectra of the first layer of FeBr₂ have no any additional components that

could be interpreted as its partial decomposition [12]. Fitting of the Fe 2p spectra for both samples yielded the same parameters (FWHM and center position). Variation of the FWHM for the Br 3p peaks (see table S1) can be attributed to the different environment of the bottom Br layer interfaced with the Au(111) surface and higher Br layers [41]. The peak ratio between the main and the satellite peaks as well as the calculated ratio for Br and Fe stays constant for both samples, supporting the presence of one single stoichiometric phase of FeBr₂ in the ordered layers epitaxially grown on Au(111).

The uniform epitaxial growth was also verified on the mesoscopic scale via LEEM and XPEEM measurements, performed at room temperature. We use the capability of LEEM microscopy and XPEEM to provide information of images with structural and chemical contrast [42], to study the 1.5-ML sample that was grown in-situ in the preparation chamber of the microscope. The bright-field LEEM image (the image obtained with a specular-00 spot) is shown in Fig. 2 (a). The contrast arises from the difference in the local reflectivity of the film with variable thickness [42]. The image represents one complete layer and large, μm -scale islands of the second layer in close accordance with the results of the STM measurements (Fig. 1 (d)) and S5). For identification of the layers we make use of the reconstruction, characteristic of the first layer

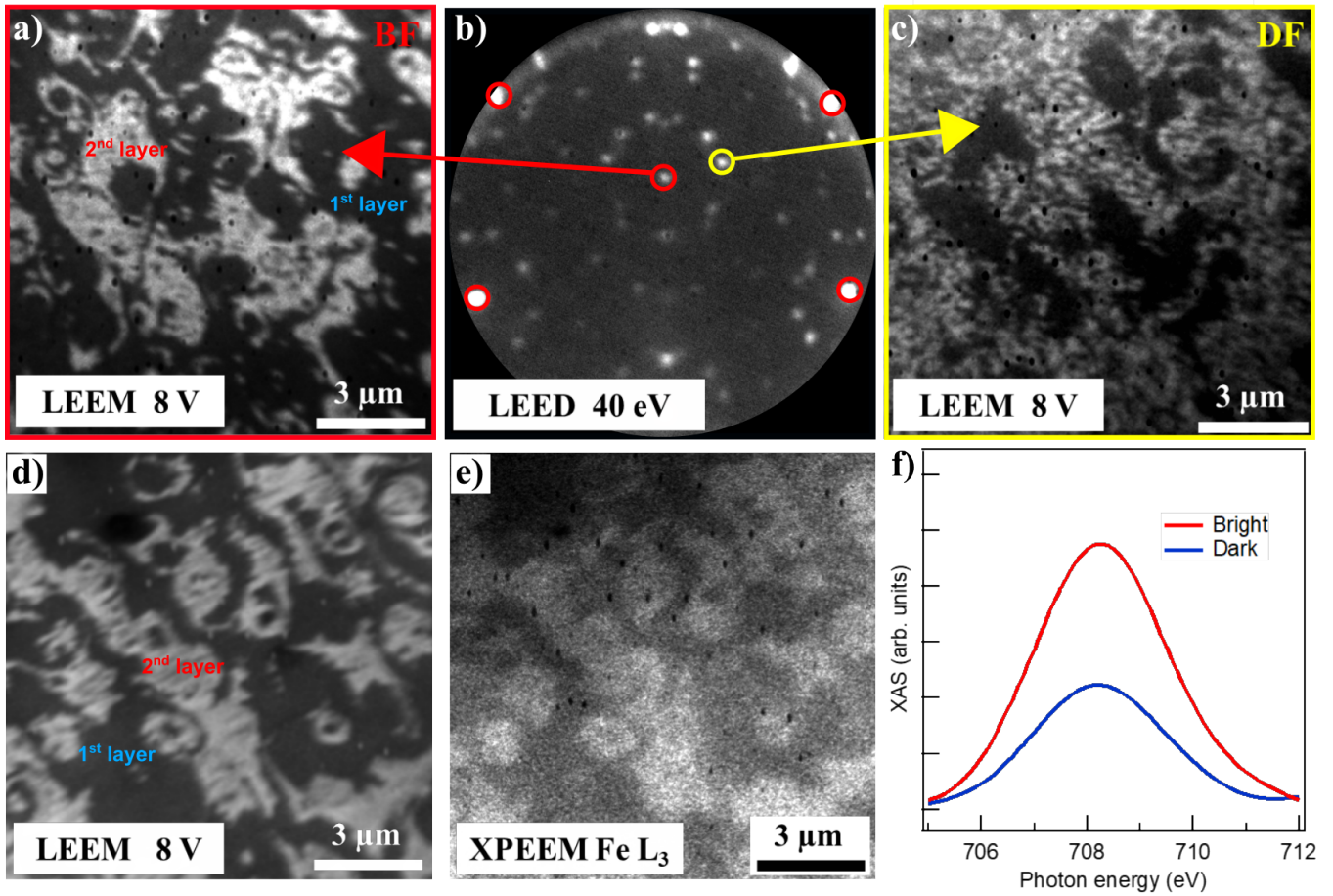


FIG. 2. LEEM and XPEEM images of 1.5 ML of FeBr_2 on $\text{Au}(111)$ at room temperature. a) Bright field (BF) LEEM image. b) μ -LEED pattern at 40 eV, red circles indicate the $\text{Au}(111)$ LEED pattern and the yellow circle marks the spot, belonging to the FeBr_2 superstructure that was used for the dark-field (DF) image. The μ -LEED pattern is distorted, since the experiment was performed with the microscope working at 10 kV, energy for which the lenses were not completely aligned in the diffraction mode, to overcome sparks during the experiment. The $\text{Au}(111)$ pattern was used as a guide to the eye to correct the distortions. c) DF-LEEM image taken at the same area as the BF image in panel a). d) Bright-field LEEM image in a different area of the sample. e) XPEEM image at the $\text{Fe } L_3$ -edge in the same area as panel d). f) Averaged intensities of the bright and dark areas of the XPEEM image e), as a function of the X-ray photon energy. The XAS spectra are obtained by taking the intensity of the image in certain points of the image.

of $\text{FeBr}_2/\text{Au}(111)$. The pattern acquired for the 1.5-ML sample with 40 eV energy of electrons (Fig. 2 (b)) is a superposition of the complex LEED pattern Fig. 1 (b) and the hexagonal pattern Fig. 1 (c), originated from the second layer of FeBr_2 . Presence of the first-order $\text{Au}(111)$ spots shows that the first layer of FeBr_2 is not perfectly continuous. Selecting a diffracted beam from the FeBr_2 superstructure, i.e. centering the illumination deflectors at that LEED spot, a dark-field image in real space was formed (Fig. 2 (c)). It has inverted contrast with respect to the BF image Fig. 2 (a). The areas with higher intensity are those that feature the reconstruction's LEED pattern (the first layer of FeBr_2). Variation of contrast within the bright zones occurs because of the presence of two rotational domains inside of the first layer of FeBr_2 (see discussion related to the Fig. 3). The large dark ar-

reas display no reconstruction. To prove that these are indeed the areas occupied with 2 ML of FeBr_2 but not the pure $\text{Au}(111)$, BF LEEM (Fig. 2 (d)) and XPEEM (Fig. 2 (e)) images were acquired at the same position.

Again, the specular (00)-spot of the LEED pattern was used for the LEEM measurements, therefore the contrast in Fig. 2 (a) and 2 (d) is the same. The XPEEM image shows the local difference in X-ray absorption at the $\text{Fe } L_3$ -edge. The averaged intensities of the bright and dark zones were calculated and represented in Fig. 2 (f) as a function of the X-ray photon energy. A larger absorption peak characteristic of the bright zones in the XPEEM image proves a higher thickness of the FeBr_2 in these areas and consequently in the bright areas of the BF LEEM images (Fig. 2 (a) and 2 (d)). Combining these results with our previous observations, we can conclude that the

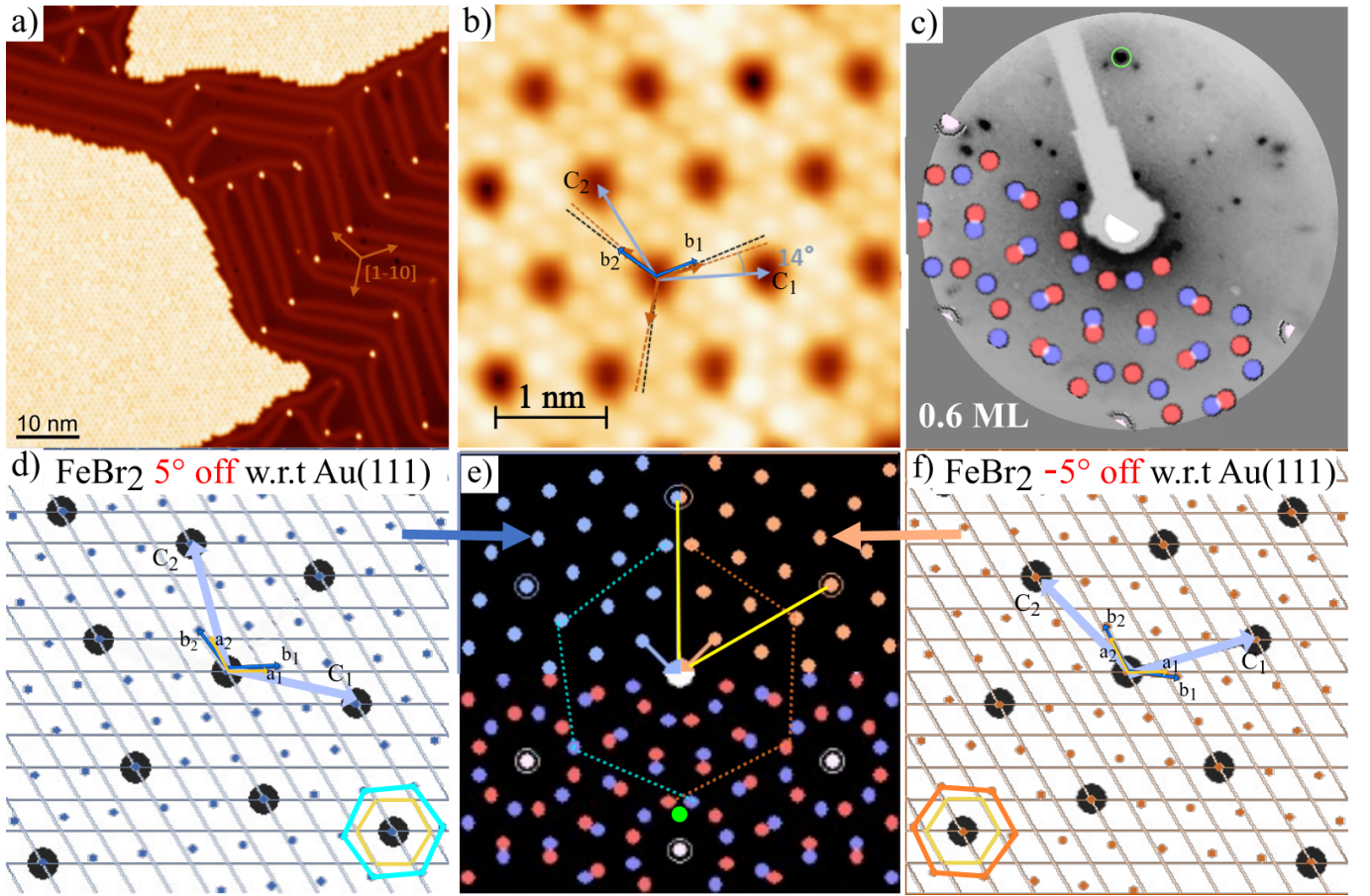


FIG. 3. (a-b) STM images of 0.6-ML of FeBr_2 at 4.3 K, measured at a) $U_{\text{Bias}}=1$ V and $I_{\text{TC}}=0.1$ nA and b) $U_{\text{Bias}}=1$ mV and $I_{\text{TC}}=1$ nA. Brown arrows indicate the close-packed Au $[1\bar{1}0]$ and equivalent directions. The superstructure unit cell (light blue arrows) and the hexagonal Br lattice unit cell (black lines) are rotated with respect to the substrate high-symmetry directions. c) LEED pattern of a 0.6-ML sample measured at 43 eV, partially overlaid with the simulated pattern. The blue and red spheres are representing the two rotational domains of the superstructure. The green circle marks one of the spots belonging to the second layer FeBr_2 hexagonal pattern. d) Relative orientation of Au(111) and rotated Br atomic nets. The lines are representing at each crossing point the position of a Au atom, the blue dots are representing the Br atoms and the dark discs mark the coincidence points (a, b and C are used to designate the respective unit cell vectors). e) shows the simulated LEED pattern of Au(111) and of the two symmetric domains of the superstructure. Yellow lines point to the Au(111) pattern, meanwhile the dashed lines show the patterns of FeBr_2 for both domains. Their relative orientation represents the configurations illustrated by two hexagons in the bottom right and bottom left corners of the panels d) and f). The green dot shows the positions of a spot belonging to the hexagonal pattern of the second layer of FeBr_2 . f) is the same as in d) but the Br grid is rotated in the opposite direction.

results of the LEEM/XPEEM characterization corroborate that the growth of FeBr_2 on Au(111) is close to the layer-by-layer mode.

Investigation of the atomic arrangement that gives rise to the reconstruction of the first layer of $\text{FeBr}_2/\text{Au}(111)$ was performed using LT-STM and LEED. The STM image displayed in Fig. 3 (a) shows two islands of FeBr_2 separated by the bare Au(111) surface with the characteristic $22 \times \sqrt{3}$ herringbone reconstruction [43, 44]. Apart of bright dots at the elbows of the herringbone probably associated with initial nucleation of FeBr_2 , the Au(111) remains clean and the FeBr_2 grows as compact ordered islands. A zoom-in image in Fig. 3 (b) reveals details of

a superstructure in the first layer of $\text{FeBr}_2/\text{Au}(111)$ with atomic-resolution. It consists of a triangular net of dark spots with periodicity of 9.7 ± 0.72 Å that obscure single Br atoms in otherwise flat layer.

Interatomic distances in the top-most Br layer were found to be of 3.66 ± 0.3 Å, in reasonable agreement with the expected monolayer lattice constant calculated by DFT [25] and the bulk value of 3.78 Å for FeBr_2 [18] (see also Fig. S4). The angle between the closed-packed directions of Au(111) and of the top-most Br plane is $\sim 5^\circ$, meanwhile the angle between the high-symmetry directions of the Au(111) and the lattice vectors of the superstructure is $\sim 14^\circ$. Fig. 3 (b) shows that the unit

vectors c_1 and c_2 of the reconstruction can be represented in terms of the unit vectors b_1 and b_2 of the Br plane as:

$$\begin{pmatrix} c_1 \\ c_2 \end{pmatrix} = \begin{pmatrix} 2 & -1 \\ 1 & 3 \end{pmatrix} \cdot \begin{pmatrix} b_1 \\ b_2 \end{pmatrix}, \quad (1)$$

where we drop the vector sign. Although the top and the bottom Br planes in the 1T structure of a single FeBr₂ slab are not equivalent, they have the same orientation of the high-symmetry directions and their lateral positions can be obtained by a rigid shift along the b_1 - b_2 direction. For the sake of clarity, we do not distinguish the top from the bottom Br planes considering relative orientation of the Br and Au(111) layers, keeping in mind this relative shift.

In Fig. 3 (d), the Au(111) plane is represented by two series of equally spaced parallel lines, crossed at 120°, and the Br plane is displayed as the set of ordered dots with six-fold symmetry. The angle between the close-packed directions of these layers is set to 5°. It is clearly seen that the vectors c_1 and c_2 constructed in accordance with Eq. (1) point to the places of coincidence between the Au(111) and the Br layers. Using the unit vectors a_1 and a_2 of the Au(111) plane, they can be represented in a matrix form as:

$$\begin{pmatrix} c_1 \\ c_2 \end{pmatrix} = \begin{pmatrix} 3 & -1 \\ 1 & 4 \end{pmatrix} \cdot \begin{pmatrix} a_1 \\ a_2 \end{pmatrix}. \quad (2)$$

These points and the equivalent ones are marked with large dark discs in the Fig. 3 (d). Calculations presented in the appendix shows that exact coincidence requires rotation of the Br layer by 5.21° and lateral expansion of the FeBr₂ by ~3% with respect to the bulk value.

The symmetry of the system requires the existence of FeBr₂ islands rotated by the same angle with respect to the Au(111) but in the opposite direction. This situation is shown in Fig. 3 (f). Representation of the unit vectors \tilde{c}_1 and \tilde{c}_2 of the coincidence points in terms of the unit vectors of the Br plane \tilde{b}_1 and \tilde{b}_2 as well as the unit vectors of the Au(111) a_1 and a_2 look like:

$$\begin{pmatrix} \tilde{c}_1 \\ \tilde{c}_2 \end{pmatrix} = \begin{pmatrix} 3 & 1 \\ -1 & 2 \end{pmatrix} \cdot \begin{pmatrix} \tilde{b}_1 \\ \tilde{b}_2 \end{pmatrix} = \begin{pmatrix} 4 & 1 \\ -1 & 3 \end{pmatrix} \cdot \begin{pmatrix} a_1 \\ a_2 \end{pmatrix}. \quad (3)$$

Fig. 3 (e) shows a simulation of the LEED pattern by means of the LEEDpat software [45]. We used Au(111) as a substrate and the superstructure visible in the STM image (Fig. 3 (b)) as the dark dots was represented by an artificial overlayer. The Au(111) unit-cell size was taken to be 2.86 Å. The overlayers were defined using the matrix relations Eq. 2 and Eq. 3, respectively. Results of the simulation for each domain are shown in the top-left and top-right quarters of Fig. 3 (e), while the bottom half of the figure shows a superposition of both patterns. We can clearly see the characteristic twelve-point circles around the central and the first-order Au(111) spots observed

in Fig. 1 (b) and 2 (b). A 43-eV LEED pattern taken for the 0.6-ML FeBr₂/Au(111) sample is shown in Fig. 3 (c). This is the same sample that was used to obtain the LEED data in Fig. 1 (b), but the superstructure pattern is much more pronounced here because of the lower energy of electrons. Half of the image is overlaid by the simulated pattern of the superstructure. An additional point highlighted with a light green circle belongs to the hexagonal pattern of the second layer of FeBr₂ (corresponding patterns in Fig. 1 (b) and (c) are marked with a blue hexagon). Since the domains of the reconstructed first layer of FeBr₂ are rotated by ±5° with respect to the gold lattice, but the second layer grows aligned with the substrate, since atomically resolved STM images of the second and third layers of FeBr₂ shown in Fig. S8 display no signs of the reconstruction of the underlying layer, we conclude that the superstructure disappears upon the growth of the higher layers.

The dark spots observed in the STM image (Fig. 3 (b)) either represent some sort of defects that follow the period of the coincidence points between the Au(111) lattice and the Br lattice of the first FeBr₂ layer or can be a pure electronic effect arising due to the interaction between the Br and Au atoms at the interface. Defects in the isostructural compound FeCl₂, which were simulated [46] and studied experimentally [38], have different appearance. We have observed similar objects as in Ref. [38] randomly distributed within the first layer of FeBr₂/Au(111) (see Fig. S4 and S6 (b)). Although we were unable to measure the bandgap, our STS data (Fig. S6 (a)) show a bump situated at 0.4 eV with respect to the Fermi level that we interpret as the onset of the conduction band (CB), meanwhile the valence band is below the range of our measurements (-2 eV). Therefore, we suggest that a monolayer of FeBr₂/Au(111) is an insulator. In this case, screening of the charge imbalance that would be the consequence of an atomic vacancy would be impeded and such a defect would affect the electronic state of the surrounding atoms. Indeed, this effect was visualised in the STM image (Fig. S6 (b)) and the corresponding conductance map, displayed in Fig. S6 (c). Furthermore, if these spots were defects, we would expect some random imperfections in their ordered structure unavoidable in any real system, which were never seen in our STM data. On the other hand, STM images of the reconstructed first layer of FeBr₂/Au(111) obtained at different values of the bias voltage do not show any change of contrast that we would expect if the dark dots of reconstruction were a purely electronic effect (see figure S7). Therefore, the mechanism leading to the reconstruction of the first layer of FeBr₂/Au(111) is not yet defined and requires further investigation.

Magnetic properties

Magnetic properties of the in-situ-grown single- and double-slab films were measured via XAS/XMCD using circularly polarized synchrotron X-ray radiation. White line (average of the spectra with left and right polarisation) absorption spectra at the Fe L_3 edge aligned to the maximum of the peak and the respective XMCD spectra are shown in Fig. 4. The structure of the XAS peak closely resembles the Fe L_3 XAS spectrum measured for FeCl_2 [47], which was attributed to the Fe^{2+} oxidation state [48, 49] (see also Fig. S11). It does not vary neither with thickness nor with temperature, which confirms the observation from the analysis of the XPS data that the films are uniform, single-phase and contain Fe^{2+} ions in the same coordination.

XMCD magnetization curves measured for different thicknesses at 2 K in two different geometries: normal incidence (NI) and grazing incidence (GI), are shown in Fig. 5 (a-b). Since they were measured in total electron yield (TEY) mode, the curves have artifact spikes around 0 T, which were removed. The loops are normalized to the Fe L_3 peak height of the respective white line (2 K, NI or GI) spectra and therefore the intensity values are proportional to the projection of the thermal average of the magnetic moment per Fe atom on the x-ray beam direction at 6 T field. The corresponding XMCD spectra are displayed as the inset in Fig. 5 (a-b). The loops do not show any field hysteresis outside the range affected by TEY artifacts and magnetization vanishes close to zero field, implying that the samples possess no simple collinear ferromagnetic ordering at that temperature.

ML	T (K)	μ ($\mu_B/\text{Fe atom}$)			
		NI		GI	
		m_{Seff}	m_l	m_{Seff}	m_l
0.6	2	1.13	0.30	1.05	0.36
1.5	2	1.814	0.60	2.03	0.45
2.0	2	2.15	0.70	1.91	0.47

TABLE I. Magnetic moments calculated by means of the sum rules from XMCD spectra obtained at $T=2$ K and $B=6$ T. Magnetic moments (μ) are divided in two sections for NI and GI. The error for each magnetic moment is $\pm 10\%$. More details about the procedure of sum-rule analysis and the extended version of the data (Table S4) are available in the supplementary information.

It was demonstrated in the previous section that growth of FeBr_2 is close to the layer-by-layer mode. Therefore the 0.6-ML sample comprises mainly one layer thick islands while the 1.5-ML and 2.0-ML samples consist of the complete first slab and islands of the second and, in minor proportion, of the third slab (see also the STM images of the 1.5-ML and 2.0-ML samples acquired at the beamline, Fig. S5). It is clearly seen from the loops

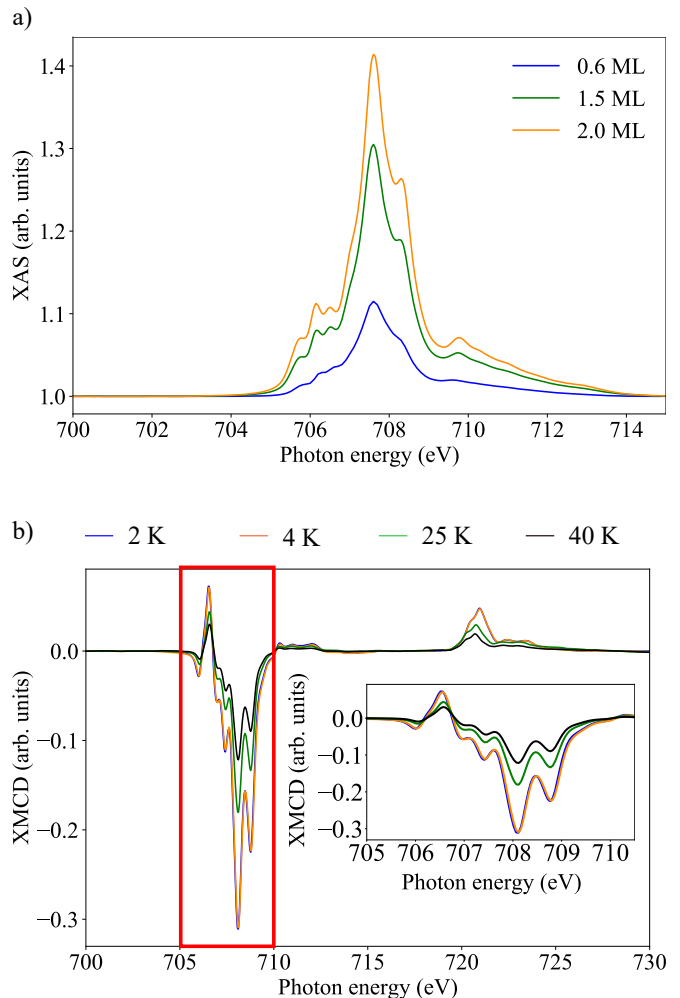


FIG. 4. a) White-line XAS spectra for different thicknesses measured at the Fe L_3 -edge, 6 T, 2 K and NI. The spectra are shifted along the energy axis to align the position of the Fe L_3 peak maxima. Further information about the shift corrections is available in the supplementary information, Fig. S10. The background subtraction was performed by using asymmetrically reweighted penalized least squares smoothing [50]. b) XMCD spectra of 2.0-ML FeBr_2 on Au(111) measured at 6 T and NI for different temperatures. The inserted image is a zoomed-in version of the L_3 region. All measurements displayed in a) and b) were performed at the BOREAS beamline.

in Fig. 5 that the expectation value of the magnetization at 2 K and 6 T along the beam direction is substantially lower in the first layer than in the thicker films. Different sub-ML samples were grown directly at the beamline and compared to the sample transferred via suitcase. Therefore, we can exclude that the reduced magnetization is a result of contamination, since all samples, also the ones grown directly at the beamline, showed a strongly reduced magnetization. Sum-rule analysis of the spectra yields values of the spin magnetic moment close to $1 \mu_B$ for the 0.6-ML sample and about $2 \mu_B$ for the 1.5-ML and 2.0-ML samples (see Table I).

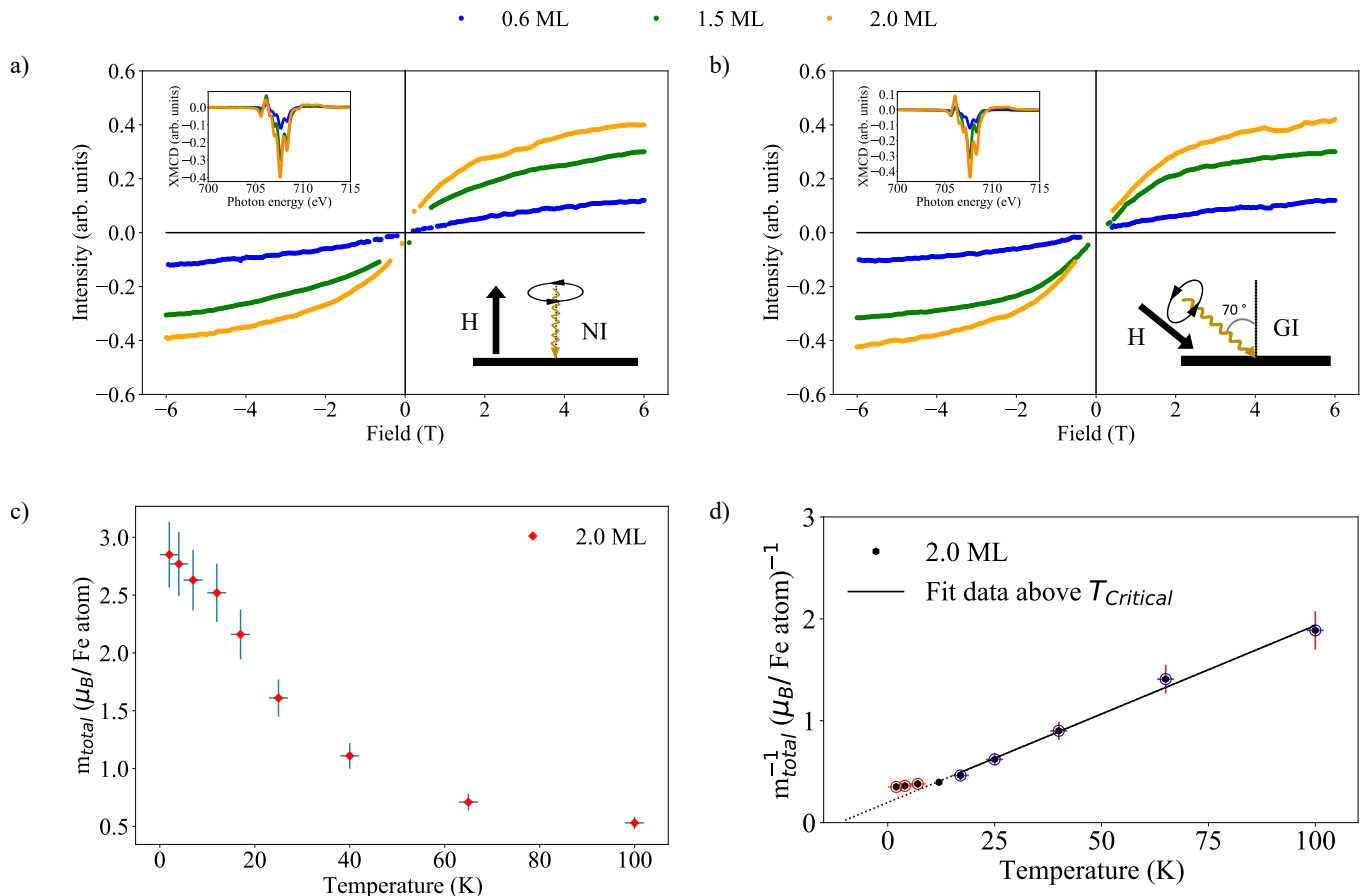


FIG. 5. Comparison of the XMCD magnetization loops for 0.6-ML, 1.5-ML and 2.0-ML $\text{FeBr}_2/\text{Au}(111)$ films measured at 2 K at: a) normal incidence (NI) and b) grazing incidence (GI) at the Fe L_3 -edge, with the field (H) parallel to the beam direction. The magnetization curves are normalized to the respective white line (averaged $(\sigma^+ + \sigma^-)/2$) XAS peak height. The insert shows the corresponding Fe L_3 XMCD peaks at 6 T and 2 K normalized to the isotropic XAS edge jump for all three samples. The magnetization loops are normalized to the maximum intensity at 6 T and multiplied by the XAS edge-jump height of the L_3 -edge. Calculated effective spin moment from the spectra of the 2.0-ML sample at 6 T and NI (c) and its inverse (d) for different temperatures. The hollow blue circles are representing the data, which were used for the linear fit of the high temperature regime ($17\text{-}100\text{ K} > T_{\text{Critical}}$). The excluded data points are displayed in red. A slope of $0.017 \pm 0.001\text{ (K} \cdot \mu_B/\text{Fe atom)}^{-1}$ and a linear intercept of $-0.198 \pm 0.049\text{ (}\mu_B/\text{Fe atom)}^{-1}$ ($\chi^2 = 0.01$) gives the estimation of the paramagnetic Curie temperature of $-10 \pm 1\text{ K}$. The chosen temperature range for the performed fit was based on the fact that the lowest used temperature is far away from saturation of a Brillouin function in a $J=2$ system. At 17 K x would be 1.9 (not in saturation see Fig. S13). All measurements displayed in a) and b) were performed at the BOREAS beamline.

Analysis of a heterogeneous magnetic system is complicated, nevertheless we can infer some additional information about magnetic ordering in the thin films of FeBr_2 from the temperature dependence of their magnetic properties. Fig. 5 shows in panels (c) and (d) the expectation value of the spin magnetic moment of the 2.0-ML sample and its inverse as a function of temperature (respective values are listed in Table S4), as obtained by sum-rule analysis of the spectra at 6 T. In the paramagnetic state, $1/m_{\text{total}}$ is proportional to the susceptibility measured in the field of 6 T, provided that the temperature is high enough to yield a linear magnetization curve. In Fig. S13, we show that for Brillouin functions with $J = 2$ and $T \geq 17\text{ K}$, this is approximately the case. Linear fitting of

the high-temperature part of this curve yields an extrapolated ordering temperature of $\sim -10\text{ K}$, well below the value of 3.5 K reported for the bulk material [16]. Its negative sign indicates the possibility of antiferromagnetic behaviour. Although a non-zero value of the extrapolated ordering temperature cannot serve as unambiguous prove, it implies that the 2.0-ML sample can be magnetically ordered at 2 K. Panel (a) of Fig. S12 shows the same total magnetic moments of the 2.0-ML sample together with curves calculated using the Brillouin function. We observe a slope change of the m_{total} vs T curve at $\sim 7\text{ K}$, in contrast to the behavior expected from a paramagnetic system with $S = 2$, supporting the presence of magnetic correlations in the 2.0-ML sample.

The magnetic behaviour of the single-layer FeBr₂ is distinctly different. Low values of the magnetic moments in an external field of 6 T as compared to the thicker films (Table I) and shallow magnetization loops in both NI and GI directions (Fig. 5) imply a magnetic order that is neither paramagnetic nor ferromagnetic. Figure S12 demonstrates that fitting of the NI 0.6-ML sample's loop to the Brillouin function does not yield satisfactory results. The paramagnetic curve at 2 K is steeper than the experimental loop and has a smaller tangent in the high-field regions. Including out-of-plane anisotropy in the model of the paramagnetic system would make it's loop even steeper. Therefore, a mere lack of magnetic order cannot explain the observed magnetic properties of a single layer of FeBr₂. STM data show that the 0.6-ML FeBr₂/Au(111) sample comprises of single layer islands with lateral size of ~ 100 nm (see Fig. 3). These islands are large enough to neglect the effect of thermal excitations at 2 K and to discard superparamagnetic behaviour. Although recent neutron diffraction data unveiled some clues of a non-collinear magnetic order in bulk FeBr₂ [51, 52], neither these nor older works [21] showed antiferromagnetic order within the layers of FeBr₂. At the same time, the intralayer exchange coupling to the nearest neighbour J_1 was found to be of different sign with respect to the next-nearest neighbour exchange coupling constant J_2 [51]. These competing interactions lead to frustration, which, according to theoretical calculations [53], can result in complex magnetic textures. The phase diagram presented in [53] demonstrates that the magnetic structure varies with the change of the J_1/J_2 ratio or due to modification of the anisotropy. Since the superstructure observed in the first layer of FeBr₂/Au(111) causes lateral expansion of the FeBr₂ crystal lattice by $\sim 3\%$ (according to our model) and the superexchange interaction depends strongly on the angle between the Fe-Br-Fe bonds, variation of the J_1/J_2 ratio can be sufficient to stabilize one of the magnetic textures predicted in [53]. On the other hand, more complex situations including a spin-glass phase or complex antiferromagnetic ordering cannot be ruled out. Although, among different possible reasons for the distinctive magnetic behaviour observed in the single-layer of FeBr₂, formation of non-collinear magnetic texture due to frustration looks rather probable, further investigations are necessary to unambiguously establish the type of magnetic structure.

Summary

Thin films (sub-ML to 2.0-ML) of FeBr₂ were grown epitaxially on a single-crystal Au(111) substrate in UHV via sublimation of the stoichiometric powder compound from a Knudsen cell. Thorough characterization performed by means of XPS and XAS/XMCD spectroscopy, as well

as via surface-sensitive LEED and LT-STM, LEEM and XPEEM shows that FeBr₂ maintains its stoichiometric chemical composition down to the single-layer limit. The growth of the films is close to the layer-by-layer mode. The first layer of FeBr₂/Au(111) demonstrates an atomic reconstruction that is interpreted as the coincidence pattern between the lattice of Br atoms in $\pm 5^\circ$ rotated domains of $\sim 3\%$ laterally expanded FeBr₂ and the Au(111) surface lattice.

XMCD measurements reveal thickness-dependent magnetic properties of the FeBr₂. While the temperature behaviour of the saturation magnetization of the second and higher layers shows some clues of magnetic ordering, magnetic properties of the single layer of FeBr₂ were found to be distinctly different. Shallow magnetization loops at 2 K, lack of saturation and low magnetization in fields up to 6 T leaves a possibility for various interpretations starting from magnetic frustration, characteristic of the triangular lattice of the magnetic Fe atoms to more complex types of magnetic order or spin-glass behaviour. These findings open the prospect for further investigation of the monolayers of the 2D magnetic transition metal dihalides. In contrast to the trihalides family that features the honeycomb arrangement of the magnetic atoms within the 2D layers, triangular nets of magnetic atoms in TMDH are prone to frustration that leads to degeneracy of the magnetic ground state and potentially may result in stronger response towards external stimuli. This quality might result in a rich variety of interesting physical phenomena and opens a way for using 2D magnetic TMDH compounds in applications.

ACKNOWLEDGMENT

C.G.-O. and M.P.-D. acknowledge funding of the Ph.D. fellowship from the MPC Foundation.

S.E.H. thanks the whole AG Kuch and in particular J. G6rdes for help during the BESSY measurements. Also he is very thankful to the local IT /electronics workshop/fine mechanics workshop team for their continuous support. In particular he is very thankful for the possibility to perform some last STM measurements at the PEARL beamline at SLS thanks to Dr. Matthias Muntwiler.

J.N. thanks the Deutsche Forschungsgemeinschaft (DFG, German Research Foundation) for his funding under the project 277101999 - CRC 183.

S.T. acknowledges financial support by the BMBF through project VEKMag (BMBF 05K19KEA).

P.G. acknowledges funding from PID2020-116181RB-C32 and FlagEraSographMEM PCI2019-111908-2 (AEI/FEDER)

D. G. O. acknowledges funding by the Spanish MCIN/AEI/ 10.13039/501100011033 and by the European Union "NextGenerationEU"/PRTR (PID2019-

107338RB-C63 and TED2021-132388B-C43).

C. R., M. I., C.G.-O. and M.P.-D. acknowledge funding by the European Union’s Horizon 2020 research and innovation programme (grant agreement No 800923), the Spanish MCIN/AEI/ 10.13039/501100011033 (PID2020-114252GB-I00, PID2019-107338RB-C63, TED2021-130292B-C42), Basque Government IT1591-22, and by the IKUR Strategy under the collaboration agreement between Ikerbasque Foundation and MPC on behalf of the Department of Education of the Basque Government.

C. R., M. I., C.G.-O. and S.E.H. are very thankful for the help during the XMCD and STM measurements of Samuel Kerschbaumer, Andrea Aguirre Baños and Amitayush Jha Thakur.

REFERENCES

* These two authors contributed equally

† Corresponding author

- [1] L. Zhang, J. Dong, and F. Ding, “Strategies, Status, and Challenges in Wafer Scale Single Crystalline Two-Dimensional Materials Synthesis,” *Chemical Reviews*, vol. 121, pp. 6321–6372, June 2021.
- [2] B. Huang, G. Clark, E. Navarro-Moratalla, D. R. Klein, R. Cheng, K. L. Seyler, D. Zhong, E. Schmidgall, M. A. McGuire, D. H. Cobden, W. Yao, D. Xiao, P. Jarillo-Herrero, and X. Xu, “Layer-dependent ferromagnetism in a van der Waals crystal down to the monolayer limit,” *Nature*, vol. 546, pp. 270–273, June 2017.
- [3] N. Sethulakshmi, A. Mishra, P. Ajayan, Y. Kawazoe, A. K. Roy, A. K. Singh, and C. S. Tiwary, “Magnetism in two-dimensional materials beyond graphene,” *Materials Today*, vol. 27, pp. 107–122, July 2019.
- [4] M. Ashton, D. Gluhovic, S. B. Sinnott, J. Guo, D. A. Stewart, and R. G. Hennig, “Two-dimensional intrinsic half-metals with large spin gaps,” *Nano Letters*, vol. 17, pp. 5251–5257, Sept. 2017.
- [5] H. Li, S. Ruan, and Y. Zeng, “Intrinsic van der waals magnetic materials from bulk to the 2d limit: New frontiers of spintronics,” *Advanced Materials*, vol. 31, p. 1900065, July 2019.
- [6] M. Gibertini, M. Koperski, A. F. Morpurgo, and K. S. Novoselov, “Magnetic 2d materials and heterostructures,” *Nature Nanotechnology*, vol. 14, pp. 408–419, May 2019.
- [7] D. L. Cortie, G. L. Causer, K. C. Rule, H. Fritzsche, W. Kreuzpaintner, and F. Klose, “Two-dimensional magnets: Forgotten history and recent progress towards spintronic applications,” *Advanced Functional Materials*, vol. 30, p. 1901414, May 2020.
- [8] W. Li, Y. Zeng, Z. Zhao, B. Zhang, J. Xu, X. Huang, and Y. Hou, “2d magnetic heterostructures and their interface modulated magnetism,” *ACS Applied Materials & Interfaces*, vol. 13, pp. 50591–50601, Nov. 2021.
- [9] Z. Zhao, W. Li, Y. Zeng, X. Huang, C. Yun, B. Zhang, and Y. Hou, “Structure engineering of 2d materials toward magnetism modulation,” *Small Structures*, vol. 2, p. 2100077, Oct. 2021.
- [10] Y. L. Huang, W. Chen, and A. T. S. Wee, “Two-dimensional magnetic transition metal chalcogenides,” *SmartMat*, vol. 2, pp. 139–153, July 2021.
- [11] S. Kezilebieke, M. N. Huda, V. Vaño, M. Aapro, S. C. Ganguli, O. J. Silveira, S. Głodzik, A. S. Foster, T. Ojanen, and P. Liljeroth, “Topological superconductivity in a van der waals heterostructure,” *Nature*, vol. 588, pp. 424–428, Dec. 2020.
- [12] D. Bikaljević, C. González-Orellana, M. Pena-Díaz, D. Steiner, J. Dreiser, P. Gargiani, M. Foerster, M. A. Nino, L. Aballe, S. Ruiz-Gomez, N. Friedrich, J. Hieuille, L. Jingcheng, M. Ilyn, C. Rogero, and J. I. Pascual, “Non-collinear magnetic order in two-dimensional NiBr₂ films grown on Au(111),” *ACS Nano*, vol. 15, pp. 14985–14995, Sept. 2021.
- [13] W. Chen, Z. Sun, Z. Wang, L. Gu, X. Xu, S. Wu, and C. Gao, “Direct observation of van der waals stacking-dependent interlayer magnetism,” *Science*, vol. 366, pp. 983–987, Nov. 2019.
- [14] B. Huang, G. Clark, D. R. Klein, D. MacNeill, E. Navarro-Moratalla, K. L. Seyler, N. Wilson, M. A. McGuire, D. H. Cobden, D. Xiao, W. Yao, P. Jarillo-Herrero, and X. Xu, “Electrical control of 2d magnetism in bilayer CrI₃,” *Nature Nanotechnology*, vol. 13, pp. 544–548, July 2018.
- [15] M. Bonilla, S. Kolekar, Y. Ma, H. C. Diaz, V. Kalappattil, R. Das, T. Eggers, H. R. Gutierrez, M.-H. Phan, and M. Batzill, “Strong room-temperature ferromagnetism in VSe₂ monolayers on van der Waals substrates,” *Nature Nanotechnology*, vol. 13, pp. 289–293, Apr. 2018.
- [16] M. McGuire, “Crystal and magnetic structures in layered, transition metal dihalides and trihalides,” *Crystals*, vol. 7, p. 121, Apr. 2017.
- [17] M. Chhowalla, H. S. Shin, G. Eda, L.-J. Li, K. P. Loh, and H. Zhang, “The chemistry of two-dimensional layered transition metal dichalcogenide nanosheets,” *Nature Chemistry*, vol. 5, pp. 263–275, Apr. 2013.
- [18] J. Haberecht, H. Borrmann, and R. Kniep, “Refinement of the crystal structure of iron dibromide, FeBr₂,” *Zeitschrift für Kristallographie - New Crystal Structures*, vol. 216, p. 510, Jan. 2001.
- [19] S. Youn, B. Sahu, and K. Kim, “Large orbital magnetic moment and coulomb correlation effects in FeBr₂,” *Physical Review B*, vol. 65, p. 052415, Jan. 2002.
- [20] S. Yang, T. Zhang, and C. Jiang, “van der waals magnets: Material family, detection and modulation of magnetism, and perspective in spintronics,” *Advanced Science*, vol. 8, p. 2002488, Jan. 2021.
- [21] M. K. Wilkinson, J. W. Cable, E. O. Wollan, and W. C. Koehler, “Neutron diffraction investigations of the magnetic ordering in FeBr₂, CoBr₂, FeCl₂, and CoCl₂,” *Physical Review*, vol. 113, pp. 497–507, Jan. 1959.
- [22] Z. Ropka, R. Michalski, and R. J. Radwanski, “Electronic and magnetic properties of FeBr₂,” *Physical Review B*, vol. 63, p. 172404, Mar. 2001.
- [23] J. Pelloth, R. A. Brand, S. Takele, M. M. Pereira de Azevedo, W. Kleemann, C. Binek, J. Kushauer, and D. Bertrand, “Local magnetic properties of antiferromagnetic FeBr₂,” *Physical Review B*, vol. 52, pp. 15372–15386, Dec. 1995.
- [24] V. V. Kulish and W. Huang, “Single-layer metal halides MX₂ (x = Cl, Br, I): stability and tunable magnetism

- from first principles and Monte Carlo simulations,” *Journal of Materials Chemistry C*, vol. 5, pp. 8734–8741, July 2017.
- [25] A. S. Botana and M. R. Norman, “Electronic structure and magnetism of transition metal dihalides: Bulk to monolayer,” *Physical Review Materials*, vol. 3, p. 044001, Apr. 2019.
- [26] M. Sargolzaei and J. Ruzs, “Spin and orbital magnetism of FeBr₂: a density functional theory study,” *Journal of Physics: Condensed Matter*, vol. 20, p. 025217, Jan. 2008.
- [27] S. Jiang, G. Wang, H. Deng, K. Liu, Q. Yang, E. Zhao, L. Zhu, W. Guo, J. Yang, C. Zhang, H. Wang, X. Zhang, J.-F. Dai, G. Luo, Y. Zhao, and J. Lin, “General synthesis of 2d magnetic transition metal dihalides via trihalide reduction,” *ACS Nano*, vol. 17, pp. 363–371, Jan. 2023. Publisher: American Chemical Society.
- [28] T. Noll and F. Radu, “The mechanics of the VEKMAG experiment,” *Proceedings of MEDSI2016*, vol. MEDSI2016, pp. 4 pages, 3.587 MB, June 2017.
- [29] A. Barla, J. Nicolás, D. Cocco, S. M. Valvidares, J. Herrero-Martín, P. Gargiani, J. Moldes, C. Ruget, E. Pellegrin, and S. Ferrer, “Design and performance of BOREAS, the beamline for resonant x-ray absorption and scattering experiments at the ALBA synchrotron light source,” *Journal of Synchrotron Radiation*, vol. 23, pp. 1507–1517, Nov. 2016.
- [30] L. Aballe, M. Foerster, E. Pellegrin, J. Nicolas, and S. Ferrer, “The ALBA spectroscopic LEEM-PEEM experimental station: layout and performance,” *Journal of Synchrotron Radiation*, vol. 22, pp. 745–752, May 2015.
- [31] H. Bana, E. Travaglia, L. Bignardi, P. Lacovig, C. E. Sanders, M. Dendzik, M. Michiardi, M. Bianchi, D. Lizzit, F. Presel, D. D. Angelis, N. Apostol, P. K. Das, J. Fujii, I. Vobornik, R. Larciprete, A. Baraldi, P. Hofmann, and S. Lizzit, “Epitaxial growth of single-orientation high-quality MoS₂ monolayers,” *2D Materials*, vol. 5, p. 035012, apr 2018.
- [32] K. V. Bets, N. Gupta, and B. I. Yakobson, “How the complementarity at vicinal steps enables growth of 2d monocrystals,” *Nano Letters*, vol. 19, no. 3, pp. 2027–2031, 2019.
- [33] S. Günther, S. Dänhardt, B. Wang, M.-L. Bocquet, S. Schmitt, and J. Wintterlin, “Single terrace growth of graphene on a metal surface,” *Nano Letters*, vol. 11, no. 5, pp. 1895–1900, 2011. PMID: 21466213.
- [34] P. Yang, S. Zhang, S. Pan, B. Tang, Y. Liang, X. Zhao, Z. Zhang, J. Shi, Y. Huan, Y. Shi, S. J. Pennycook, Z. Ren, G. Zhang, Q. Chen, X. Zou, Z. Liu, and Y. Zhang, “Epitaxial growth of centimeter-scale single-crystal MoS₂ monolayer on Au(111),” *ACS Nano*, vol. 14, no. 4, pp. 5036–5045, 2020. PMID: 32267670.
- [35] M. Newville, T. Stensitzki, D. B. Allen, and A. Ingargiola, “LMFIT: Non-linear least-square minimization and curve-fitting for python,” Jan. 2014.
- [36] L. Martín-García, I. Bernal-Villamil, M. Oujja, E. Carrasco, R. Gargallo-Caballero, M. Castillejo, J. F. Marco, S. Gallego, and J. de la Figuera, “Unconventional properties of nanometric FeO(111) films on Ru(0001): stoichiometry and surface structure,” *Journal of Materials Chemistry C*, vol. 4, no. 9, pp. 1850–1859, 2016.
- [37] T. Yamashita and P. Hayes, “Analysis of XPS spectra of Fe²⁺ and Fe³⁺ ions in oxide materials,” *Applied Surface Science*, vol. 254, pp. 2441–2449, Feb. 2008.
- [38] X. Zhou, B. Brzostowski, A. Durajski, M. Liu, J. Xi-ang, T. Jiang, Z. Wang, S. Chen, P. Li, Z. Zhong, A. Drzewiński, M. Jarosik, R. Szczeniński, T. Lai, D. Guo, and D. Zhong, “Atomically thin 1T-FeCl₂ grown by molecular-beam epitaxy,” *The Journal of Physical Chemistry C*, vol. 124, no. 17, pp. 9416–9423, 2020.
- [39] P. S. Bagus, C. J. Nelin, C. R. Brundle, B. V. Crist, N. Lahiri, and K. M. Rosso, “Origin of the complex main and satellite features in Fe 2p xps of Fe₂O₃,” *Physical Chemistry Chemical Physics*, vol. 24, pp. 4562–4575, 2022.
- [40] J. F. Moulder, *Handbook of X-ray photoelectron spectroscopy: a reference book of standard spectra for identification and interpretation of XPS data*. Perkin-Elmer Corporation, update ed., 1992.
- [41] H. Bana, E. Travaglia, L. Bignardi, P. Lacovig, C. E. Sanders, M. Dendzik, M. Michiardi, M. Bianchi, D. Lizzit, F. Presel, D. De Angelis, N. Apostol, P. Kumar Das, J. Fujii, I. Vobornik, R. Larciprete, A. Baraldi, P. Hofmann, and S. Lizzit, “Epitaxial growth of single-orientation high-quality MoS₂ monolayers,” *2D Materials*, vol. 5, p. 035012, Apr. 2018.
- [42] J. I. Flege and E. E. Krasovskii, “Intensity–voltage low-energy electron microscopy for functional materials characterization,” *Physica Status Solidi (RRL) – Rapid Research Letters*, vol. 8, no. 6, pp. 463–477, 2014.
- [43] C. J. Murphy, X. Shi, A. D. Jewell, A. F. McGuire, D. O. Bellisario, A. E. Baber, H. L. Tierney, E. A. Lewis, D. S. Sholl, and E. C. H. Sykes, “Impact of branching on the supramolecular assembly of thioethers on Au(111),” *The Journal of Chemical Physics*, vol. 142, p. 101915, Mar. 2015.
- [44] K. Schouteden, P. Lievens, and C. Van Haesendonck, “Fourier-transform scanning tunneling microscopy investigation of the energy versus wave vector dispersion of electrons at the Au(111) surface,” *Physical Review B*, vol. 79, p. 195409, May 2009.
- [45] K. Hermann and M. A. Van Hove, “Leedpat, version 4.2.”
- [46] E. Ceyhan, M. Yagmurcukardes, F. M. Peeters, and H. Sahin, “Electronic and magnetic properties of single-layer FeCl₂ with defects,” *Physical Review B*, vol. 103, p. 014106, Jan. 2021.
- [47] J. Everett, E. Céspedes, L. R. Shelford, C. Exley, J. F. Collingwood, J. Dobson, G. van der Laan, C. A. Jenkins, E. Arenholz, and N. D. Telling, “Ferrous iron formation following the co-aggregation of ferric iron and the Alzheimer’s disease peptide β -amyloid (1–42),” *Journal of The Royal Society Interface*, vol. 11, p. 20140165, June 2014.
- [48] J. K. Kowalska, B. Nayyar, J. A. Rees, C. E. Schiewer, S. C. Lee, J. A. Kovacs, F. Meyer, T. Weyhermüller, E. Otero, and S. DeBeer, “Iron L_{2,3} -edge x-ray absorption and x-ray magnetic circular dichroism studies of molecular iron complexes with relevance to the FeMoCo and FeVCo active sites of nitrogenase,” *Inorganic Chemistry*, vol. 56, pp. 8147–8158, July 2017.
- [49] P. S. Miedema and F. M. de Groot, “The iron L edges: Fe 2p x-ray absorption and electron energy loss spectroscopy,” *Journal of Electron Spectroscopy and Related Phenomena*, vol. 187, pp. 32–48, Apr. 2013.
- [50] S.-J. Baek, A. Park, Y.-J. Ahn, and J. Choo, “Baseline correction using asymmetrically reweighted penalized least squares smoothing,” *The Analyst*, vol. 140, pp. 250–257, Sept. 2014.
- [51] K. Katsumata, H. A. Katori, S. M. Shapiro, and G. Shi-

- rane, “Neutron-scattering studies of a phase transition in the metamagnet FeBr₂ under external magnetic fields,” *Physical Review B*, vol. 55, pp. 11466–11470, May 1997.
- [52] C. Binek, T. Kato, W. Kleemann, O. Petracic, D. Bertrand, F. Bourdarot, P. Burllet, H. A. Katori, K. Katsumata, K. Prokes, and S. Welzel, “Neutron scattering study of transverse magnetism in the metamagnet FeBr₂,” *The European Physical Journal B - Condensed Matter and Complex Systems*, vol. 15, pp. 35–40, May 2000.
- [53] A. O. Leonov and M. Mostovoy, “Multiply periodic states and isolated skyrmions in an anisotropic frustrated magnet,” *Nature Communications*, vol. 6, p. 8275, Sep 2015.